INDERSCIENCE PUBLISHERS
Linking academia, business and industry through research

International Journal of Vehicle Design

ISSN online: 1741-5314 - ISSN print: 0143-3369
https://www.inderscience.com/ijvd

The optimisation design of CFRP bumper beam based on ply compatibility

Jing Chen, Sen Xu, Zhen Liu, Aotian Tang, Wei Lv

DOI: 10.1504/IJVD.2024.10061814

Article History:

Received:	29 June 2020
Last revised:	30 April 2021
Accepted:	25 May 2022
Published online:	23 January 2024

The optimisation design of CFRP bumper beam based on ply compatibility

Jing Chen, Sen Xu*, Zhen Liu and Aotian Tang

State Key Laboratory of Automobile Simulation and Control (ASCL),
Jilin University,
Changchun, Jilin Province, 130022, China
Email: cjing@jlu.edu.cn
Email: x2500914998@163.com
Email: autotat@163.com
Email: aizhenl@163.com
*Corresponding author

Wei Lv

China FAW Corporation Limited Jiefang Business Division
Commercial Vehicle Development Institute,
Changchun, Jilin Province, 130011, China
Email: lvwei@rdc.faw.com.cn

Abstract: In recent years, the global car ownership has continued to grow. In order to reduce the energy consumption rate of automobiles and improve the driving dynamics of automobiles, automobile lightweight technology has been widely used in the automobile industry. At the same time, with the continuous development of new material technology, various low-density and high-strength materials (aluminium alloy, high-strength steel, carbon fibre, basalt fibre, glass fibre, etc.) are gradually being used in some parts of automobiles. The purpose of this paper is to carry out the lightweight and optimal design of the carbon fibre reinforced polymer front bumper beam of the automobile by optimising the ply design of the carbon fibre reinforced polymer bumper beam based on the compatibility of the laminate layup. Compared with the traditional steel bumper beam, it has finally achieved 47.61% weight reduction while ensuring the collision performance.

Keywords: bumper beam; carbon fibre reinforced polymer; ply compatibility; lightweight design; optimisation algorithm.

Reference to this paper should be made as follows: Chen, J., Xu, S., Liu, Z., Tang, A. and Lv, W. (2024) 'The optimisation design of CFRP bumper beam based on ply compatibility', *Int. J. Vehicle Design*, Vol. 94, Nos. 1/2, pp.100–122.

Biographical notes: Jing Chen is a Professor of State Key Laboratory of Automotive Simulation and Control and Automotive Engineering, Jilin University, Changchun, China. She received her PhD in Automotive Engineering from the Jilin University in 2002. Her main research areas include design and manufacture for lightweight structure, structural optimisation and evolutionary optimisation algorithm, and NVH analysis and control.

Sen Xu is a MS candidate at the Jilin University in Automotive Engineering. His research interests include automotive lightweight structure and evolutionary optimisation algorithm.

Zhen Liu is a MS candidate at the Jilin University in Automotive Engineering. His research interests include automotive lightweight structure and evolutionary optimisation algorithm.

Aotian Tang is a MS candidate at the Jilin University in Automotive Engineering. His research interests include automotive lightweight structure and evolutionary optimisation algorithm.

Wei Lv is an Automotive Engineer in China FAW Corporation Limited Jiefang Business Division Commercial Vehicle Development Institute. His main research areas are structural design and optimisation.

1 Introduction

The lightweight technology has caused a considerable improvement in mechanical structures via three main methods (Zuoet al., 2016a): structural optimisation, lightweight material, and advanced technology. Considerable research on lightweight design and application in vehicle structures has been conducted in recent years. Fauzi et al. (2018) adopted a crashbox made of a carbon fibre-reinforced polymer composite (CFRP) with double-hat thin-walled constructions and conducted a crashworthiness experiment and a simulation analysis of composite-based crashbox structures. Cho et al. (2016) used material selection and size optimisation methods to derive a lightweight composite hybrid carbody design. Koch et al. (2017) presented two approaches to reducing the weight of electric motor rotors, comprising a hybrid shaft made of carbon-reinforced plastic and stainless steel and the replacement of electric sheets with soft magnetic compounds (iron-filled polyamide compounds).

Bumper beam is main structural component of an automobile bumper subsystem that absorbs energy during a collision. It is expected to be sufficiently deformable to absorb the collision energy and reduce the risks of injury for front or rear ends of passengers. In the optimisation of traditional steel-made bumpers, the main purpose is to optimise the section and thickness of the components (Qian et al., 2016; Sun et al., 2017). Tanlak et al. (2015) investigated the optimal shape design of a bumper beam and optimised the beam by using a hybrid search algorithm to improve its crashworthiness in low- and high-velocity impact. The results showed that the strain energy absorbed by the optimal beam was improved by 16%. Belingardi et al. (2015) and Beyene et al. (2014) studied both materials and manufacturing solution for a bumper beam with evaluation criteria such as impact energy, maximum force, crash resistance, energy absorption, and stiffness. Bumpers with honeycomb designs (Soni and Pradhan, 2019) were proposed for crashworthiness improvement and enhanced energy absorbing capacity. Godara and Narayan Nagar (2020) designed the frontal bumper beam with eight different cross sections, and displacement and stress analysis at low speed collision was achieved.

In comparison with isotropic materials, composite materials were composed of two or more components providing enhanced properties compared with each component individually. Their low mass and high strength were perfectly suited for various industries, such as the aerospace field and automobile. However, they have a wider range of parameters influencing structural behaviour. Ply orientation (Basri et al., 2019; Lakshmi Kumari et al., 2018), fibre volume fraction, stacking sequence (Nikbakt et al., 2018; Solis et al., 2018), fibre material, matrix type and ply thickness (Caminero et al., 2018) are examples of these effective parameters that affect the performance of laminate structures. Design variables tend to be huge with complex optimisation problems occur when applying these materials. Meanwhile, they promote the development and application of optimisation algorithms, such as improved genetic algorithms (GAs) and multiobjective particle swarm optimisation (MOPSO) (Mohammed et al., 2017; Tian and Shi, 2018). Linearly weighted average method, and geometrically averaged cost function method are also efficient in resolving optimisation problems. Besides, surrogate models are common methods widely used in many other multiobjective optimisation problems for lightweight or crashworthiness optimisation, it usually including radial basis function (RBF) (Xiong et al., 2017), response surface methodology (RSM) (Fang et al., 2017), artificial neural network (ANN) (Baykasoglu and Baykasoglu, 2017), gene expression programming (GEP) (Baykasoglu and Baykasoglu, 2016), and Kriging interpolation method. For its effect in reducing computing burdens in optimisation process, it has attracted attention in the engineering field.

This paper mainly studied the optimisation of ply sequence and thickness in each ply area of a CFRP bumper beam. After the accuracy of a finite element model (FEM) was verified, it was used to obtain the optimum parameter combination of a B-shaped section. Different from the current ply optimisation methods for composite bumper beams, which are always dedicated to the stepwise optimisation design of ply sequence and thickness, a ply optimisation method considering ply compatibility principle was proposed. During the process of ply optimisation, the multi-island GA (MIGA) and the MOPSO algorithm based on Kriging model (KMOPSO) with adding-point strategy were used to derive the optimum ply design scheme of each ply area. The collision performance was enhanced and the goal of lightweight was achieved after optimisation. Then, the bench test and a three-point bending experiment were conducted to check the variation in the simulation and test after optimisation. From the comparative results, it has showed that the optimisation process was accurate and credible.

2 Establishment and verification of finite element model

On the basis of the constructed geometric model, the FE model of the front end structure of a vehicle was built with Belytschko–Tsay thin-shell elements on HyperMesh. As shown in Figure 1, it was meshed using shell elements of 10 mm (28862 elements), and all freedom, except the translation of X-direction, was constrained. The contact between the bumper beam and the energy-absorbing boxes was defined as single surface contact, while the contact between the beam and collider was defined as surface to surface contact. The static and dynamic friction coefficients were set to 0.2. The spotwelds

among different parts had MAT100 as material and were simulated using a beam element.

Figure 1 Simplified model of vehicle front end structure (see online version for colours)

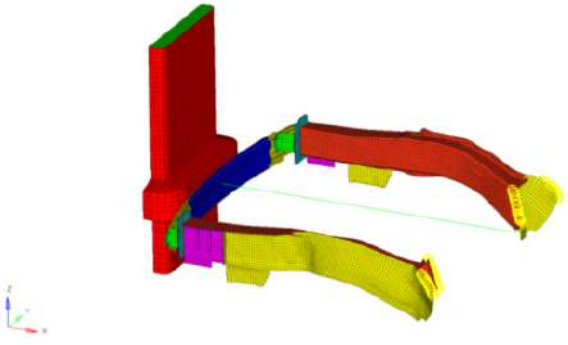

Firstly, a high-speed collision was conducted to verify the correctness of the constructed FE model of the bumper beam. In accordance with the C-NCAP(2012) test standard, a crashworthiness test of 100% overlap frontal rigid barrier (100%FRB) was conducted with a velocity of 50 km/h. The test point M was arranged in the middle of the bumper beam, as illustrated in Figure 2. Figure 3(a) and (b) depict the deformation in the simulation and test. Both in simulation or experiment, the front steel-made beam of the car shows the same deformation trend after the collision.

Figure 2 Measuring point arrangement of bumper beam (see online version for colours)

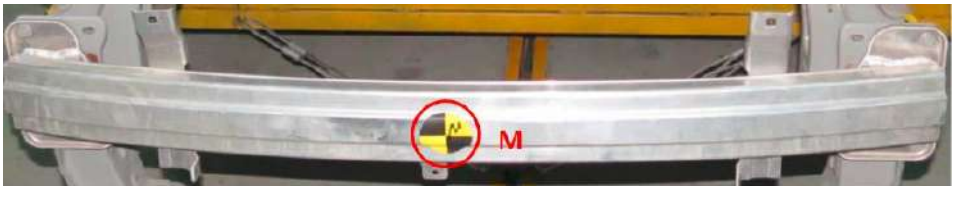

Figure 3 Deformation of simulation and test: (a) simulation and (b) test (see online version for colours)

(a) (b)

3 Section design of the CFRP bumper beam

Bumper beam was manufactured using several CFRP material plies with a thickness of 0.2 mm. The corresponding mechanical properties are provided in Table 1. As shown in Figure 4, this paper focused on the common B-shaped cross-section design. Distinction of two sections of B shape was through the positive and negative values of parameter b. The left was defined as negative, whereas the right was positive.

Figure 4 Different B-shaped cross-sections of bumper beam (see online version for colours)

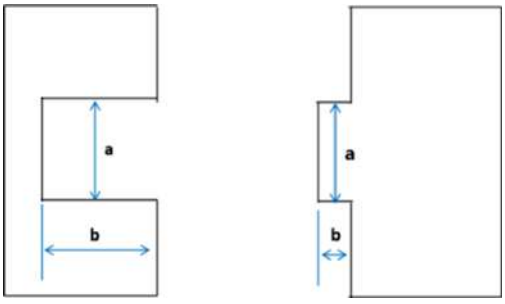

Table 1 Mechanical properties of the CFRP material

Constants	*Value*	*Constants*	*Value*
E_1/GPa	181	X_t/MPa	1500
E_2/GPa	10.3	X_c/MPa	1500
μ	0.287	Y_t/MPa	40
G_{12}/GPa	7.17	Y_c/MPa	246
G_{23}/GPa	7.17	S/MPa	68

The orthogonal experimental design method (Zuo et al., 2016b; Jiaqiang et al., 2018), which qualitatively analyses the correlations among relevant variables at different levels, was used to acquire the best parameter combination of the selected cross section. Before an orthogonal design table was made, reasonable and representative levels of all factors were determined first (Table 2). Then, orthogonal experiments displayed in the orthogonal table L_{16} (2^4) (Table 3), which presents all the level groups of the experimental factors, were performed to study the impact degrees of positive and negative factors on objectives by calculating intrusion, energy absorption, and impact force. The extreme difference analysis (Table 4), which is performed to reflected the influence degree of factors on indexes also help determine the optimal conditions.

Table 2 Orthogonal factor level

Factor level	*a/mm*	*b/mm*
1	240	40
2	320	60
3	400	−340
4	480	−360

Table 3 Results of the orthogonal experiment

Factor trial number	*a*	*B*	*Impact force/kN*	*Intrusion/mm*	*Energy absorption/J*
1	a_1	b_1	8.950	73.432	347.276
2	a_1	b_2	9.642	83.223	266.299
3	a_1	b_3	13.357	65.189	412.299
4	a_1	b_4	12.755	65.385	416.963
5	a_2	b_1	8.964	82.311	352.366
6	a_2	b_2	9.272	74.074	358.765
7	a_2	b_3	13.144	65.262	419.695
8	a_2	b_4	13.668	65.239	416.619
9	a_3	b_1	15.533	80.395	236.257
10	a_3	b_2	16.365	59.561	430.315
11	a_3	b_3	13.732	68.085	400.130
12	a_3	b_4	8.486	66.549	409.325
13	a_4	b_1	14.282	69.385	358.852
14	a_4	b_2	12.610	81.192	352.262
15	a_4	b_3	15.561	67.384	429.632
16	a_4	b_4	12.142	61.885	431.816

Table 4 Results of extreme difference analysis

Evaluation index	*Maximum energy absorption/J*		*Maximum section impact force/kN*		*Intrusion/mm*	
Average value	*Factor a*	*Factor b*	*Factor a*	*Factor b*	*Factor a*	*Factor b*
$\overline{y}_{j1}$	360.709	323.688	11.176	11.932	71.807	76.381
$\overline{y}_{j2}$	386.861	351.910	11.262	11.972	71.722	74.513
$\overline{y}_{j3}$	369.007	415.439	13.529	13.949	68.648	66.480
$\overline{y}_{j4}$	393.141	418.681	13.649	11.763	69.962	64.765
R_j	32.432	94.993	2.473	2.186	3.159	11.616
Excellent level	a_4	b_4	a_1	b_4	a_3	b_4
Primary and secondary factors	$b > a$		$a > b$		$b > a$	
Optimal combination	a_4b_4		a_1b_4		a_3b_4	

From the result in Table 4, it can be observed that:

- Factor b had more influence on the collision performance than factor a.
- For factor b, b_4 was the optimal level toward all evaluate indexes of collision performance.
- For factor a, the optimal level corresponding to each index differed.

The optimal combination of each index was further compared. Combination a_4b_4 could maintain the moderate section impact force while ensuring the minimum intrusion and the maximum energy absorption of the CFRP bumper beam. Hence, section parameter a was set to 480 mm, while parameter b was set to –360 mm.

4 Multiobjective optimisation design of CFRP bumper beam

4.1 Ply compatibility proposal for CFRP bumper beam

Evidence indicates that modifying fibre orientations within composite materials, which form the components, enable structures to have increased resistance to delamination failure and improve the impact strength. That means ply orientation and sequence have a significant effect on composite component. Both orientation and sequence of ply should not be decided arbitrarily, the following manufacturing constraints must be satisfied first when laying the bumper beam.

Symmetry constraint: The ply of the laminated plate was symmetrical about the middle plane.

External surface ply constraint: The external surface of ply structure must be continuous, which means the fibre ply orientation of component external surface should be identical.

Limit of adjacent lost plies: The maximum number of the lost plies in the adjacent area of plies was not allowed to exceed 4.

Principle of ply compatibility: The thinnest module of ply areas should maximise the number of shared plies.

Continuity constraint of ply number: The number of consecutive plies with the same ply orientation angle should not exceed 3.

As demonstrated in Figure 5, we divided the ply area into four parts: front, rear, top, and bottom.

Usually, the consideration of single-area ply led to the following issues:

- The unreliable connection at the transition point among different ply areas caused interruption in force transmission and insufficient rigidity of the CFRP bumper beam.
- Excessive design variables caused challenges in obtaining the algorithm solution.

A ply compatibility scheme based on parallel optimisation of ply stacking sequence and thickness was proposed to resolve above problems. Ply in the area with the minimum layup thickness was considered to be a shared layup, and other layups are inserted in

accordance with the principle of laminate layup under the minimum layup thickness to obtain different layup thicknesses that meet the principle of layup compatibility.

Figure 5 Different B-shaped cross-sections of bumper beam

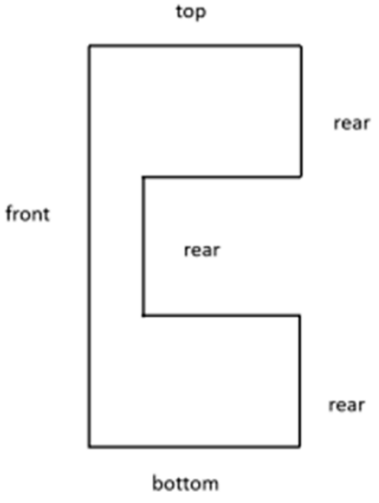

4.2 Multiobjective optimisation of ply sequence under various ply thicknesses

Ply sequences typically involved a combination of four ply angles: 0°, ±45°, and 90°. The angles were relative to the main loading direction of the applied load. The factors of CFRP ply thickness included 1.2, 1.6, 2.0, and 2.4 mm. The thickness of a single carbon fibre ply laminate was 0.2 mm, that is, when a symmetrical ply method was used, the numbers of design variables included in the thickness of 1.2, 1.6, 2.0, and 2.4 mm were 3, 4, 5, and 6, respectively. Each variable had four laying angles and optimal Latin hypercube sampling design with a minimum deviation of 64 groups was implemented for each thickness factor. The Kriging surrogate model (Jeonget al., 2005) was adopted to replace the simulation analysis with a mathematical function for minimising the time of scientific analysis and improving the optimisation efficiency. Accuracy of the established surrogate model was measured using the degree of deviation from the coefficient of determination (R^2) (Table 5). The full-factorial test with 1.2 mm thickness was conducted without bias; thus, its R^2 value was 1.

Table 5 Coefficient of determination value of response approximation model with various thickness factors

	R^2		
Ply thickness/mm	*Intrusion amount/mm*	*Maximum section impact force/kN*	*Maximum energy absorption/J*
1.6	0.9771	0.9443	0.9529
2.0	0.9531	0.9374	0.9344
2.4	0.9780	0.9373	0.9437

From Table 6, it suggested that coefficient of determination of various thickness factors were close to 1, and the predicted values of the surrogate model did not deviate substantially from the true response in allowable range. The Kriging surrogate model built, whose accuracy had been verified, could be applied for subsequent optimisation design.

Table 6 Comparison of algorithm solution and simulation results

		Energy absorption/J		*Maximum impact force/kN*		*Intrusion/mm*	
Thickness	*Ply sequence*	*Algorithm value*	*Simulation result*	*Algorithm value*	*Simulation result*	*Algorithm value*	*Simulation result*
2.4 mm	$(45°/90°/0°/-45°/90°/0°)_s$	435.233	432.474	14.767	15.830	55.959	54.706
2.0 mm	$(45°/0°/-45°/90°/0°)_s$	439.398	434.352	12.270	12.756	69.380	67.344
1.6 mm	$(45°/0°/-45°/90°)_s$	417.760	417.760	11.153	11.153	69.053	69.053
1.2 mm	$(45°/-45°/90°)_s$	424.925	424.925	8.225	8.225	92.730	92.730

The objective of the lightweight optimisation design was to minimise the section impact force under each thickness, as indicated in equation (1). The constraint was to ensure the intrusion and the energy absorption less than limited value. With the manufacturing constraints of ply design considered simultaneously, the mathematical model of the frontal impact optimisation design was set as follows:

$$\begin{cases} \textit{Minimize} \quad f(\boldsymbol{x}) = (f_F^{2.4}(\boldsymbol{x}), f_F^{2.0}(\boldsymbol{x}), f_F^{1.6}(\boldsymbol{x}), f_F^{1.2}(\boldsymbol{x})) \\ \textit{Variable} \quad \boldsymbol{x} = [x_1, x_2, x_3, x_4, x_5, x_6]^T \\ \textit{Subject to} \quad g_E^{1.2}(\boldsymbol{x}), g_E^{1.6}(\boldsymbol{x}), g_E^{2.0}(\boldsymbol{x}), g_E^{2.4}(\boldsymbol{x}) \geq 400 \\ \qquad\qquad g_D^{1.2}(\boldsymbol{x}), g_D^{1.6}(\boldsymbol{x}), g_D^{2.0}(\boldsymbol{x}), g_D^{2.4}(\boldsymbol{x}) \leq 80 \\ \qquad\qquad g_c \\ \qquad\qquad x_i \in \{0^\circ, 90^\circ, \pm 45^\circ\} \end{cases} \tag{1}$$

where x_i represents the variables of ply thickness; $f_F^{1.2}$, $f_F^{1.6}$, $f_F^{2.0}$, and $f_F^{2.4}$ are the maximum section impact forces when each ply thickness was adopted in bumper beam; $g_E^{1.2}$, $g_E^{1.6}$, $g_E^{2.0}$, and $g_E^{2.4}$ represent the maximum values of energy absorption during a collision; and g_c is the compatibility constraint among each ply thickness.

Based on the symmetry constraint, surface ply constraint, limit of adjacent lost plies, and continuity constraint of ply number, which were considered in the optimisation design period, the concrete scheme of ply design was introduced.

In order to maximise the shared ply, if the ply sequence under 2.4 mm thickness was $(x_1, x_2, x_3, x_4, x_5, x_6)_s$, then the ply sequences under 2.0 mm thickness might be $(x_1, x_3, x_4, x_5, x_6)_s$ or $(x_1, x_2, x_4, x_5, x_6)_s$ or $(x_1, x_2, x_3, x_5, x_6)_s$ or $(x_1, x_2, x_3, x_4, x_6)_s$, and $(x_1, x_2, x_3, x_4,$

$x_5)_s$. If the ply sequence at 2.0 mm thickness was $(x_1, x_3, x_4, x_5, x_6)_s$, then the ply sequences at 1.6 mm thickness might be $(x_1, x_4, x_5, x_6)_s$ or $(x_1, x_3, x_5, x_6)_s$ or $(x_1, x_3, x_4, x_6)_s$ or $(x_1, x_3, x_4, x_5)_s$. If the ply sequence of 1.6 mm thickness was $(x_1, x_4, x_5, x_6)_s$, then the ply sequences at a thickness of 1.2 mm might be $(x_1, x_5, x_6)_s$ or $(x_1, x_4, x_6)_s$ or $(x_1, x_4, x_5)_s$. That is, once the ply sequence was determined for each set of 2.4 mm thickness, with different thickness combinations, there are a total of 60 sets of layup plans to meet the compatibility of the layup. For a set of ply scheme with different thickness combinations abovementioned, the ply sequences of the first and last layers were identical, accompanied with the continuous surface of the bumper beam. Also, maximum number of ply loss in adjacent ply areas was less than 4, which met the principle of maximum ply loss and weakest module was considered a shared ply stacking. If design variables of 2.4 mm thickness was defined as $(x_1, x_2, x_3, x_4, x_5, x_6)_s$, 2.0 mm was $(x_1, x_3, x_4, x_5, x_6)_s$, 1.6 mm was $(x_1, x_4, x_5, x_6)_s$, and 1.2 mm was $(x_1, x_5, x_6)_s$, then the mathematical formula for the ply continuity was set as follows:

$$
\begin{aligned}
&g_c^{\,i}\begin{cases} d; & z_i(\boldsymbol{x}) > 0 \\ 0; & z_i(\boldsymbol{x}) = 0 \end{cases} \\
&z_{2.4}(\boldsymbol{x}) = l(x_5 = x_6) + l(x_1 = x_3 = x_4 = x_5) + l(x_1 = x_3 = x_4 = x_5) \\
&z_{2.0}(\boldsymbol{x}) = l(x_5 = x_6) + l(x_1 = x_3 = x_4 = x_5) \\
&z_{1.6}(\boldsymbol{x}) = l(x_5 = x_6) \\
&z_{1.2}(\boldsymbol{x}) = l(x_5 = x_6)
\end{aligned}
\tag{2}
$$

where d is an constant penalty value, it was used when the rule of continuity constraint of ply number was violated. The values of i represent thickness of 1.2, 1.6, 2.0, and 2.4. $z_{2\cdot4}(\boldsymbol{x})$, $z_{2\cdot0}(\boldsymbol{x})$, $z_{1\cdot6}(\boldsymbol{x})$, and $z_{1\cdot2}(\boldsymbol{x})$ are functions used for judging whether the continuity constraint is satisfied under the thicknesses of 2.4, 2.0, 1.6, and 1.2 mm, respectively. $l(.)$ is the indicator function; if it is true, it is set to 1; otherwise, it is set to 0.

Each objective usually conflicted with others in the multiobjective problem. Multiobjective optimisation methods based on preference were adopted in this study. The decision was made first, then the search was carried out. Multiobjective problem was transformed into a single-objective problem by linear weighting among the objectives, that is,

$$
f(\boldsymbol{x}) = 0.25 \cdot f_{F1.2}(\boldsymbol{x}) + 0.25 \cdot f_{F1.6}(\boldsymbol{x}) + 0.25 \cdot f_{F2.0}(\boldsymbol{x}) + 0.25 \cdot f_{F2.4}(\boldsymbol{x}) \tag{3}
$$

The mathematical problem mentioned above could be solved via MIGA.MIGA (Weimin et al., 2019; Seo et al., 2014; Kim et al., 2018; Peikun and Zhenpo, 2016) was a modified algorithm of parallel distributed GAs. Compared with traditional GAs, it has superior global solving capacity, computational efficiency, and convergence capability. Individual populations are divided into subgroups called ‘islands’. This division is the main feature of MIGA that distinguishes itself from traditional GA. All traditional genetic operations, including selection, crossover, and mutation, are performed independently on each island. After a series of genetic operations, some individuals are selected from some islands and migrated to different islands periodically. The island of migration is selected randomly, and individuals are exchanged among selected islands in accordance with the migration rate.

The formula shown in equation (4), in which the fitness function is set to the sum of the product of the objective function, the dynamic penalty function coefficient, and the static penalty function.

$$\begin{aligned} g_p(\boldsymbol{x}) &= \sum_{l=1}^{k} h_l(\boldsymbol{x}) \\ h(\boldsymbol{x}) &= \begin{cases} a_i \left| g_i(\boldsymbol{x}) - b_i \right|; & g_i(\boldsymbol{x}) > b_i \\ 0; & g_i(\boldsymbol{x}) \le b_i \end{cases} \\ y_g(\boldsymbol{x}) &= f(\boldsymbol{x}) + c \cdot (g_p(\boldsymbol{x}) + g_c) \\ c &= 10^{(1-p)} \\ p &= \sum_{j=1}^{n} l(g_p(\boldsymbol{x}) + g_c \neq 0) \end{aligned} \tag{4}$$

where $g_p(\boldsymbol{x})$ is a penalty value for out-of-bounds performance corresponding to a set of ply schemes with different ply thicknesses, k represents number of thickness used for layup, a_i is the penalty coefficient of the ith evaluation index, $h(x)$ is the penalty value considering all evaluation index of each ply thickness, $g_i(\boldsymbol{x})$ is the ith evaluation index constraint function value which is provided by surrogate model, b_i is the threshold of the ith evaluation index constraint function, $y_g(\boldsymbol{x})$ represents the fitness function of a set of ply scheme, c is the coefficient of the dynamic adaptive penalty function, p is the sum of individual number in the previous iteration that violated the constraints, n is the population size, and l (.) is the indicator function (if it is true, it is set to 1; otherwise, it is set to 0).

Sixty sets of fitness function values could be obtained if a design variable of thickness 2.4 mm is determined. To unite the fitness function form and promote algorithm efficiency, $y(\boldsymbol{x})$ in equation (5) was used as the final fitness function by employing the minimum value of 60 sets of ply schemes.

$$y(\boldsymbol{x}) = Min(y_g^1(\boldsymbol{x}), y_g^2(\boldsymbol{x}), y_g^3(\boldsymbol{x}), \cdots, y_g^{60}(\boldsymbol{x})) \tag{5}$$

where $y(\boldsymbol{x})$ is the final fitness function of design variables. $y_g{}^1(\boldsymbol{x})$, $y_g{}^2(\boldsymbol{x})$, $y_g{}^3(\boldsymbol{x})$,…, $y_g{}^{6\circ}(\boldsymbol{x})$ represent fitness values of 60 different sets of ply combinations.

The best combination of ply sequence of each thickness was determined via programmed MIGA. Optimisation result is shown in Table 6 by comparing the simulation values with algorithm results.

Simulation results of evaluation indexes of 1.2 and 1.6 mm thickness were identical with the algorithm optimisation result. For the thickness factors of 2.0 and 2.4 mm, the maximum percentage error between the simulation results of each indicator and the optimisation results of algorithm did not exceed 7%.

4.3 Multiobjective optimisation of ply thickness under determined ply sequence

In the optimisation algorithm based on surrogate model, the design of experiment (DOE) was an essential segment which conducted preliminary scans of design space and obtained the change law with few trials, thus providing information on the different spatial positions and representative basic data of the surrogate model to be constructed. As the research continued, the role of the surrogate model had changed. It was no longer

a simple substitution but constituted an optimisation mechanism based on historical data to enable the addition of sample points and generate local or global optimal solutions.

EGO algorithm (Viana et al., 2012) includes the Kriging model to use the prediction value information and the deviation information of the prediction value to complete the optimisation. Current existing swarm intelligence optimisation algorithm commonly applies the information of predicted value to complete the optimisation. In the Kriging model, the provided predicted deviation of its own estimation information makes the optimisation algorithm remove the solution with a large deviation in predicted value and improve the optimisation efficiency. Combing the swarm intelligence optimisation algorithm with the EGO algorithm and used the Kriging model as a vinculum. An optimisation algorithm, KMOPSO, was proposed.

As we all know, the steps of traditional PSO are outlined as follows:

Step 1: A problem is defined, and a swarm of particles with stochastic positions xi and velocities vi in n-dimensional space is initialised.

Step 2: The fitness value for each particle is calculated and evaluated, pbest of each particle is regarded as its current position, and gbest is set equal to the position of the most superior initial particle.

Step 3: The position and velocity of all particles in the swarm are updated.

Step 4: pbest and gbest of each particle are updated in accordance with fitness value and Pareto domination.

In the swarm intelligence optimisation algorithm, each particle has memory and maintains a record of its previous personal best position (*pbest*) with its fitness. Considerable *pbest* is available for specific particles in the swarm, and the particle with greatest fitness is called the global best (*gbest*) of the swarm.

After the particle's position information is updated as described in Step 3 above, not only its speed and position should be checked whether beyond the boundary, but also its fitness function should be updated by equation (6). At the same time, compared with the fitness function corresponding to the optimal position of particle individual in the previous iteration, the dominant individual is set as the personal best.

$$\begin{aligned} F_i &= f_i(\boldsymbol{x}) + \lambda_i \max(0, g_i(\boldsymbol{x})) \\ f(\boldsymbol{x}) &= \left[f_1(\boldsymbol{x}), f_2(\boldsymbol{x}), \cdots, f_m(\boldsymbol{x})\right] \\ g(\boldsymbol{x}) &= \left[g_1(\boldsymbol{x}), g_2(\boldsymbol{x}), \cdots, g_n(\boldsymbol{x})\right] \end{aligned} \tag{6}$$

where F_i is the constructed fitness function include two parts. The first element in equation (6) is the *i*th objective function of particle, and the latter part is the penalty term, which is composed of penalty coefficient λ_i and constraint function.

If current individual and the optimal individual do not dominate each other, then use the deviation information $\overline{V_i}$ (shown in equation (7)) provided by the surrogate model. Individual with smaller cumulative deviation is determined as the personal best.

$$
\begin{aligned}
f_k^s(\boldsymbol{x}) &= \sqrt{\sigma^2\{\mathbf{1}-\boldsymbol{r}_{f_k}^T\boldsymbol{R}_{f_k}^{-1}\boldsymbol{r}_{f_k}+(\mathbf{1}-\boldsymbol{r}_{f_k}^T\boldsymbol{R}_{f_k}^{-1}\boldsymbol{r}_{f_k})^2/\boldsymbol{F}_{f_k}^T\boldsymbol{R}_{f_k}^{-1}\boldsymbol{F}_{f_k}\}} \\
g_t^s(\boldsymbol{x}) &= \sqrt{\sigma^2\{\mathbf{1}-\boldsymbol{r}_{g_t}^T\boldsymbol{R}_{g_t}^{-1}\boldsymbol{r}_{g_t}+(\mathbf{1}-\boldsymbol{r}_{g_t}^T\boldsymbol{R}_{g_t}^{-1}\boldsymbol{r}_{g_t})^2/\boldsymbol{F}_{g_t}^T\boldsymbol{R}_{g_t}^{-1}\boldsymbol{F}_{g_t}\}} \\
V_k^i &= \frac{(f_k^s)_i-(f_k^s)_{min}}{(f_k^s)_{max}-(f_k^s)_{min}} \quad V_t^i = \frac{(g_t^s)_i-(g_t^s)_{min}}{(g_t^s)_{max}-(g_t^s)_{min}} \\
\overline{V}_i &= \sum_{k=1}^{m} V_k^i + \sum_{t=1}^{n} V_t^i
\end{aligned}
\tag{7}
$$

where σ^2 represents the variance value, $\boldsymbol{r}$ is the correlation coefficient vector between undiscovered and sample points, and $\boldsymbol{R}$ is the correlation matrix function of sample point. f_k^s represents the deviation function of the kth objective function, and g_t^s represents the deviation function of the tth constraint function (Intrusion, Energy absorption). V_k^i is the normalised value of the deviation function of the ith particle to the kth objective function, and V_t^i is the normalised deviation value of the tth constraint function of the ith particle. $\overline{V}_i$ is the cumulative deviation of the ith particle.

The concept of gbest is particularly important in PSO because it indicates the most ideal solution received by the entire swarm. Position of gbest is the area where all particles in the iteration focus on exploring and appropriate gbest should be selected to complete social learning:

- Comparison of non-dominant relationship: the non-dominant individuals determined in this iteration are compared with the global best in the last iteration, and a non-dominant repository is obtained by comparing the dominant relationships based on fitness function
- Construction mechanism of external repository: As the iterative process proceeds, increasing non-dominated solutions are found using PSO and stored in the external repository through dominance comparison. When the number of non-dominated solutions in the repository reaches the upper limit, the dynamic crowding distance (CD) maintenance strategy will be used to decide whether a member of a repository needs to be replaced. In the proposed algorithm, the capacity of the repository is defined in advance, and all candidates are temporarily stored in it. In the iterative process, the selection process of non-dominated solutions can be summarised as follows:
- When the number of non-dominated solutions in the repository does not exceed the maximum size limit, all non-dominated particles are stored in the repository.
- When the number of non-dominated solutions in the repository reaches the maximum size limit, the CD (shown in equation (8)) of each non-dominated solution needs to be solved and ranked via the strategy for dynamic CD, and one particle with the smallest value is removed. The above operation is repeated until non-dominated solutions reach the maximum size limit of the repository.

$$D_i = \sum_{j=1}^{m} \left| \frac{f_j^{i+1} - f_j^{i-1}}{f_j^{max} - f_j^{min}} \right| \qquad \overline{D}_i = \frac{D_i - D_{min}}{D_{max} - D_{min}} \tag{8}$$

where the superscript i represents the number of particles, the subscript j indicates the order of objective function. D_i is the crowding distance of the ith particle and $\overline{D}_i$ is the normalised value.

The particles in repository that met the conditions of $\overline{D}_i > 0.7$ and $\overline{V}_i < 0.8$ were defined as *gbest* to ensure that the particles had a large crowding distance and a small cumulative deviation, thereby improving the accuracy of the solution of nondominated fronts.

Many algorithms have good convergence properties, which are usually achieved by the cost of diversity. The mutation operation (shown in) seems to be essential to explore the search space to a great extent while attaining enhanced diversity.

$$x_{i'} = x_i + (v_p^M - v_p^m) \cdot rand \cdot \left(1 - 0.9 \cdot \frac{t}{MP}\right) \tag{9}$$

where MP is the total number of iterations, t is the current iteration number, $x_i^{'}$ is the position information after the mutation. $v_p{}^M$ and $v_p{}^m$ represent the upper and lower limits of the speed of the ith particle with respect to the pth variable, respectively.

The expected improvement (EI) sampling criterion is one of the most popular infill criteria and is used to balance local and global search. EI shows the potential of being smaller (or bigger) than the current minimum (or maximum) value in a minimisation (or maximisation) problem and considers the predicted function value and its uncertainty at the same time. This feature allows exploring the design space globally. In the adding-point strategy, at the end of each round of optimisation, the normalised cumulative function deviation of each particle in the Pareto front is exploited, and the particles in the front solution that meet the condition $\overline{V}_i < 0.3$ are set as the approximately real Pareto front solution. EI criterion add points in the front solution set according to the EI function below:

$$EI_k^j = (f_k^j - \overline{y}_k(\boldsymbol{x})) \cdot \psi\left(\frac{f_k^j - \overline{y}_k(\boldsymbol{x})}{f_k^s(\boldsymbol{x})}\right) + f_k^s(\boldsymbol{x}) \cdot \varphi\left(\frac{f_k^j - \overline{y}_k(\boldsymbol{x})}{f_k^s(\boldsymbol{x})}\right)$$
$$EIM = \min_{j=1}^{q} \sqrt{\sum_{k=1}^{m} (EI_k^j)^2} \tag{10}$$

where Ψ and Φ are the standard distribution and normal density, respectively. $\overline{y}_k(\boldsymbol{x})$ is the predicted value of the kth objective function through the Kriging model. f_k^j is an element in the jth row k-column of the approximate real Pareto front solution, and f_k^s is the deviation of the predicted value of the kth objective function.

Particle with the biggest EIM value was added to the design space. As the round of algorithm iterations increased, the accuracy of the model improved.

This algorithm terminated after executing a specified number of iterations. Procedure of KMOPSO with adding-point strategy is displayed in flowchart (Figure 6).

Figure 6 Flowchart of *KMPSO* algorithm

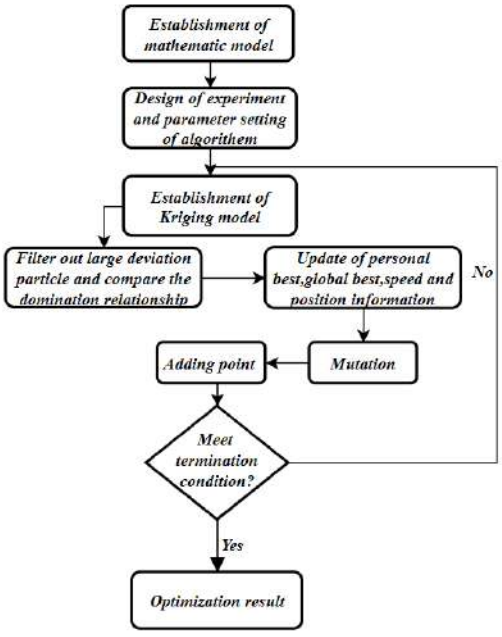

In accordance with the algorithm procedure, the mathematical model of the optimisation problem was constructed firstly.

$$\begin{cases} Variable & x_i = [x_1, x_2, x_3, x_4]^T \\ Min & f(\boldsymbol{x}) = (f_F(\boldsymbol{x}), f_M(\boldsymbol{x}), -f_E(\boldsymbol{x})) \\ Subject\ to & g_D(\boldsymbol{x}) \le 80 \\ & x_i \in \{1.2, 1.6, 2.0, 2.4\} \end{cases} \tag{11}$$

where x_1, x_2, x_3, and x_4 represent the ply thickness of top, bottom, front, and rear ply areas, respectively. $f_M(\boldsymbol{x})$, $f_E(\boldsymbol{x})$, $f_F(\boldsymbol{x})$ and $g_D(\boldsymbol{x})$ represent mass, energy absorption, impact force of section, and intrusion function respectively.

As for energy absorption function, the maximum value is always expected, but the algorithm solution is usually set as the minimum value. Thus, the opposite value was considered.

After DOE, the accuracy of the Kriging surrogate model built with the values of absolute coefficient R^2 should be evaluated. Coefficient of determination (R^2) of Kriging surrogate model for each evaluation index of one ply thickness is shown in Figure 7, from which the errors of R^2 were less than 10%. It was sufficiently accurate to be utilised to execute further iteration optimisation.

Figure 7 Coefficient of determination of surrogate model for evaluation indexes of a ply thickness: (a) energy absorption; (b) impact force and (c) intrusion (see online version for colours)

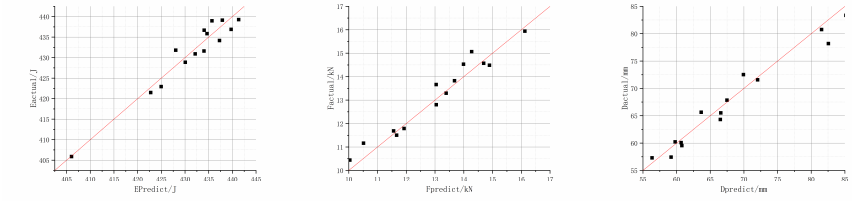

(a) (b) (c)

Pareto front (Figure 8) was ultimately exported after several rounds of iteration. Meanwhile, the optimum thickness of each ply area and corresponding values of evaluation index was achieved as follows:

$$[x_1, x_2, x_3, x_4] = [1.2, 1.2, 1.6, 2.0 \text{ mm}].$$

$$[f_M(\boldsymbol{x}), f_E(\boldsymbol{x}), f_F(\boldsymbol{x}), g_D(\boldsymbol{x})] = [1.216 \text{ kg}, 14.890 \text{ kN}, 435.492 \text{ J}, 56.492 \text{ mm}].$$

Figure 8 Pareto front of multiobjective optimisation (see online version for colours)

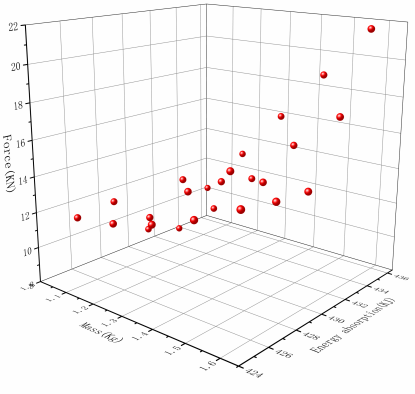

4.4 Performance of the optimised CFRP bumper beam

As shown in Figure 9, optimised CFRP bumper beam was simulated both at low and high speed. At 40 ms (Figure 9(a)), the bumper beam began to deform under an impact force. It gradually reached the maximum deformation at 80 ms (Figure 9(b)), and the impact velocity was nearly 0 km/h at the moment. At 120 ms (Figure 9(c)), bumper beam recovered elastically with reduction in intrusion. Then, it was out of contact with the rigid wall at 160 ms (Figure 9(d)), which revealed the termination of the collision process.

Figure 9 Low-speed collision simulation deformation diagram of optimised CFRP bumper beam (see online version for colours)

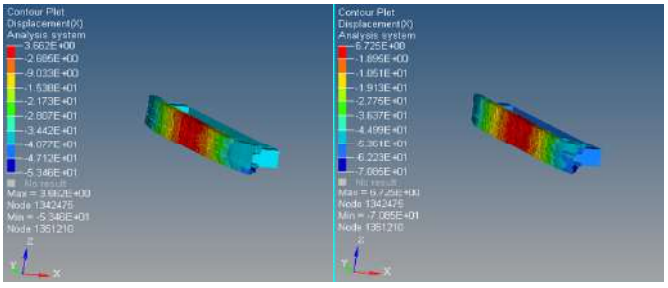

(a) (b)

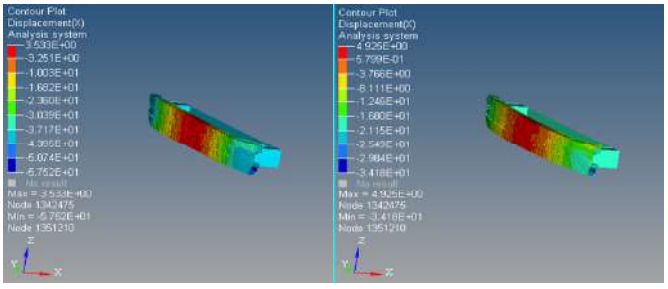

(c) (d)

Performance analysis was conducted based on the weight reduction, the maximum intrusion, the maximum section force of energy-absorbing box, and the maximum energy absorption of bumper beam. Figure 10(a) indicates the maximum energy absorption (439.254 J), the growth rate of which was 2.3% compared with that of a steel-made beam (429.262 J). The reduction in section force was apparent with a rate of 15.78% (Shown in Figure 10(b)). Also, intrusion of the optimised beam compared with that of the steel-made beam was decreased by 21.31% (Figure 10(c)), which demonstrated the excellent optimisation effect.

Figure 10 Comparison curves of *CFRP* bumper beam in low speed collision (see online version for colours)

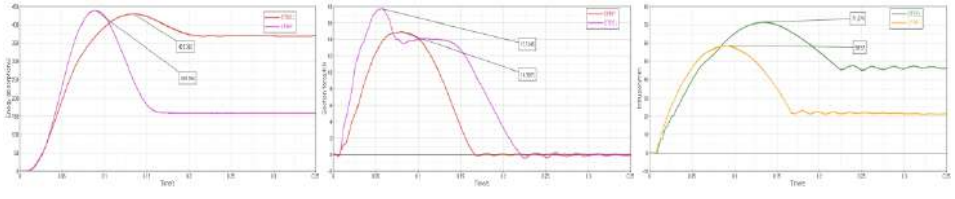

(a) (b) (c)

The optimised CFRP bumper beam was also used for the simulation analysis of 50 km/h high-speed collision test, and the deformation diagram of the front end structure was provided (Figure 11).

Figure 11 Deformation of high speed collision simulation (see online version for colours)

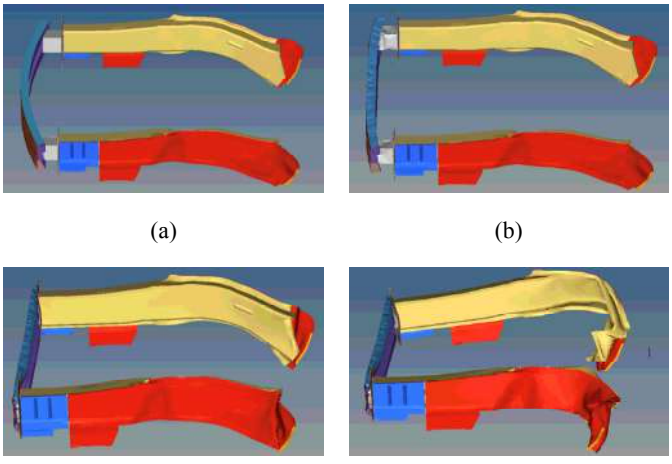

(a) (b)

(c) (d)

In the high-speed collision, accompanying with minimal deformation of the energy-absorbing box, the beam initially deform between 0 ms and 7.5 ms (Figure 11(a)). Between 7.5 ms and 17.5 ms (Figure 11(b)), the energy-absorbing box was gradually crushed, and the deformation of the front longitudinal beam was small and front longitudinal beam began to deform greatly meanwhile, then the CFRP bumper beam and energy-absorbing box were completely crushed between 17.5 ms and 35 ms (Figure 11(c)).

From Figure 11, the CFRP bumper beam, energy-absorbing box, and front longitudinal beam were crushed in a correct sequence in the whole process, and the deformation situation was also reasonable.

5 Bench test verification and three-point bending test

Optimised bumper beam, energy-absorbing box, and fixture were connected to an experimental trolley, which was weighted to ensure sufficient kinetic energy (Figure 12). The collider (shown in Figure 1) has changed into a rigid wall and sensors was arranged on the trolley to record information of points attached to the energy-absorbing box (Figure 13). After the preparatory work, a 100% FRB crashworthiness test at a speed of 4 km/h was performed.

Figure12 Real vehicle test preparation: (a) connections of CFRP bumper beam and (b) the experiment trolley (see online version for colours)

(a) (b)

Figure 13 Measuring points arrangement (see online version for colours)

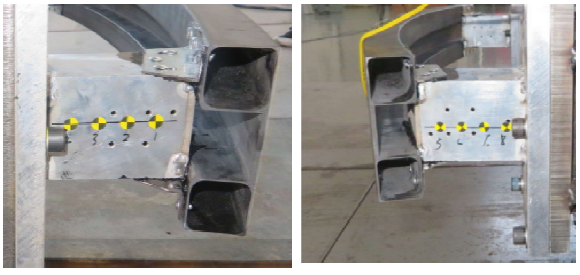

Compared with result of the collision simulation of FE model constructed under same experimental condition. The percentage error of maximum test impact force was 11.28% (Figure 14). Meanwhile, the maximum intrusion was 58.0235 mm at 78 ms in the test and 54.4067 mm at 83 ms in the simulation (Figure 15). Time difference between the simulation and test was only 5 ms when the maximum intrusion was reached and the intrusion error was 3.6168 mm with a percentage error of 6.69%. Curves in both simulation and test were consistent.

Figure 14 Comparison curves of impact force for simulation and substantial vehicle test (see online version for colours)

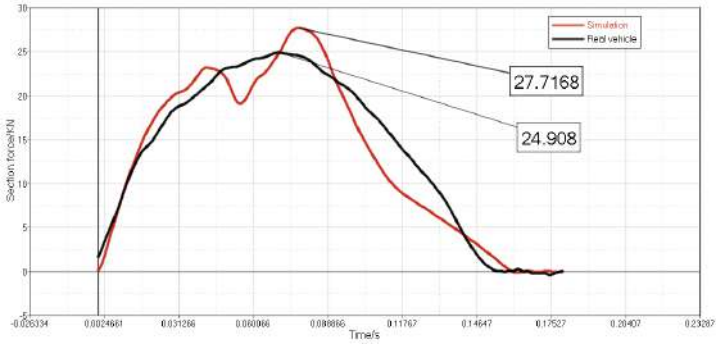

The three-point bending test was performed in a quasi-static condition, and the span of two fixed ends was set to 919.3 mm, which was the distance of the inner side points of

energy-absorption boxes. Velocity of the drop hammer was set to 2 mm/min. Sensors were arranged on the test platform to extract the force and displacement information in the impact process. When the drop hammer started contacting the bumper, its position was photographed using a high-speed video camera.

Figure 15 Comparison curves of intrusion for simulation and substantial vehicle test (see online version for colours)

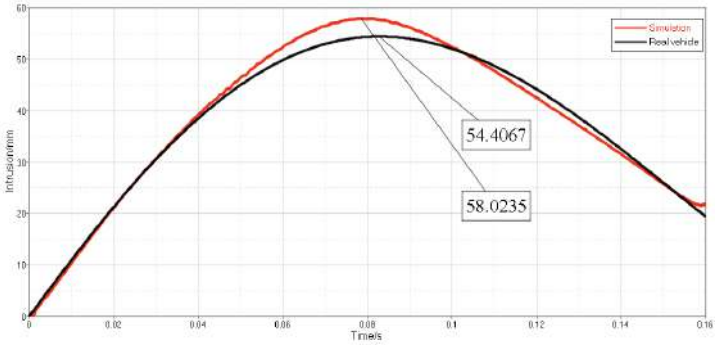

Simultaneously, a simulation analysis of the FE model built with the identical experimental condition was conducted, and the result was obtained for a comparison with the test value (Figure 16). The structure of the bumper beam had not been exactly damaged at 3 min, but evident deformation (reaching 7.728 mm) had occurred (Figure 16(a) and (b)). At 9 min, the arc of the bumper beam had been flattened half, and the deformation had reached 19.87 mm. Eventually, the deformation had reached 42.51 mm and bumper beam was broken (Figure 16(c) and (d)).

Figure 16 Three point bending deformation diagram of simulation and test (see online version for colours)

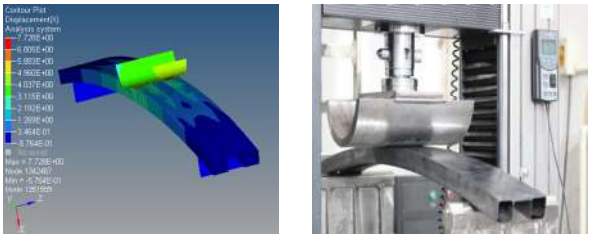

(a) (b)

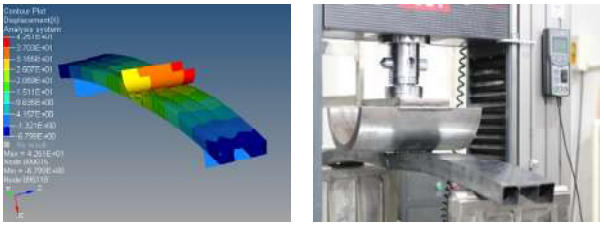

(c) (d)

From curves of force and displacement extracted from the sensors (Figure 17), the CFRP bumper beam was damaged with the maximum displacement (40.0899 mm) and the maximum reaction of supports (22.1596 kN) in the test, and the CFRP bumper beam was damaged with the maximum displacement (42.5117 mm) and the maximum reaction of supports (24.3483 kN) in the simulation. The simulation and test error of the maximum displacement was 5.7%, and the simulation and test error of the maximum reaction force was 8.99%. It has a little deviation but within allowable range, which demonstrated that the force and displacement curves in the simulation and test were highly consistent.

Figure 17 Force and displacement curves in simulation and test (see online version for colours)

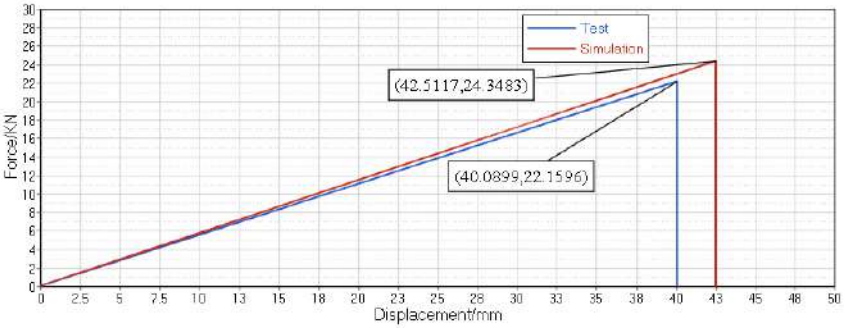

6 Conclusion

In this study, a ply structural optimisation method considering ply compatibility principle for a CFRP bumper beam was proposed. An innovative algorithm (KMOPSO) used to solve multiobjective optimisation issues was successfully applied to improve the crashworthiness and lightweight performance of the bumper beam.

The optimal parameter of the determined section with B shape was obtained through the application of an orthogonal experimental design. Through optimisation included ply sequence under various ply thicknesses, and the ply thickness under the determined ply sequence. The optimal ply result of the CFRP bumper beam was eventually derived.

Low-speed collision simulation of the optimised beam suggested that the maximum section force decreased by 15.78% compared with that of the unoptimised CFRP beam, and the intrusion and absorbed energy were obviously improved compared with those of a traditional steel-made beam. From comparative result of both three-point bending test and low-speed bench test, it proved that the trend of curves was similar in the test and simulation, which demonstrated that the process of multiobjective optimisation was reliable and credible, and the goal of lightweight was ultimately achieved with 47.61% mass reduction.

Acknowledgements

Authors would like to acknowledge the National Key Research and Development project of China (2016YFB0101601) and Jilin Province and Jilin University jointly sponsor special foundation (SXGJSF2017-2-1-5).

References

Basri, E.I., Sultan, M.T.H.M.F., Basri, A.A., Abas, M.F., Majid, M.S.A. and Ahmad, K.A. (2019) 'Performance analysis of composite ply orientation in aeronautical application of unmanned aerial vehicle (UAV) NACA4415 wing', *Journal of Materials Research and Technology*, Vol. 8, pp.3822–3834.

Baykasoglu, A. and Baykasoglu, C. (2016) 'Crashworthiness optimization of circular tubes with functionally-graded thickness', *Engineering Computations* (*Swansea, Wales*), Vol. 33, pp.1560–1585.

Baykasoglu, A. and Baykasoglu, C. (2017) 'Multiple objective crashworthiness optimization of circular tubes with functionally graded thickness via artificial neural networks and genetic algorithms', *Proceedings of the Institution of Mechanical Engineers, Part C: Journal of Mechanical Engineering Science*, Vol. 231, pp.2005–2016.

Belingardi, G., Beyene, A.T., Koricho, E.G. and Martorana, B. (2015) 'Alternative lightweight materials and component manufacturing technologies for vehicle frontal bumper beam', *Composite Structure*, Vol. 120, pp.483–495.

Beyene, A.T., Koricho, E.G., Belingardi, G. and Martorana, B. (2014) 'Design and manufacturing issues in the development of lightweight solution for a vehicle frontal bumper', *Procedia Engineering*, Vol. 88, pp.77–84.

Caminero, M.A., García-Moreno, I. and Rodríguez, G.P. (2018) 'Experimental study of the influence of thickness and ply-stacking sequence on the compression after impact strength of carbon fibre reinforced epoxy laminates', *Polymer Testing*, Vol. 66, pp.360–370.

Cho, J.G., Koo, J.S. and Jung, H.S. (2016) 'A lightweight design approach for an EMU carbody using a material selection method and size optimization', *Journal of Mechanical Science and Technology*, Vol. 30, pp.673–681.

Fang, J., Sun, G., Qiu, N., Kim, N.H. and Li, Q. (2017) 'On design optimization for structural crashworthiness and its state of the art', *Structural and Multidisciplinary Optimization*, Vol. 55, pp.1091–1119.

Fauzi, F.R., Hadi, B.K., Santosa, S.P. and Jusuf, A. (2018) 'Composite based lightweight structure design for crash and safety application', *2018 5th International Conference on Electric Vehicular Technology (ICEVT)*, 30–31 October, Surakarta, Indonesia, pp.161–166.

Godara, S.S. and Narayan Nagar, S. (2020) 'Analysis of frontal bumper beam of automobile vehicle by using carbon fiber composite material', *Materials Today: Proceedings*, https://doi.org/10.1016/j.matpr.2020.02.550

Jeong, S., Murayama, M. and Yamamoto, K. (2005) 'Efficient optimization design method using kriging model', *2005 IEEE Congress on Evolutionary Computation, IEEE CEC 2005 Proceedings*, Vol. 3, pp.2138–2145.

Jiaqiang, E., Han, D., Qiu, A., Zhu, H., Deng, Y., Chen, J. and Peng, Q. (2018) 'Orthogonal experimental design of liquid-cooling structure on the cooling effect of a liquid-cooled battery thermal management system', *Applied Thermal Engineering*, Vol. 132, pp.508–520.

Kim, S., Kim, K. and Son, C. (2018) 'Adaptation method for overall and local performances of gas turbine engine model', *International Journal of Aeronautical and Space Sciences*, Vol. 19, pp.250–261.

Koch, S-F., Peter, M. and Fleischer, J. (2017) 'Lightweight design and manufacturing of composites for high-performance electric motors', *Procedia CIRP*, Vol. 66, pp.283–288.

Lakshmi Kumari, N.B.V., Mehar, A., Abdulrahman, M., Tatineni, S., Venkateshwara Shashank, E. and Ted Muthyala, J. (2018) 'Performance analysis of ply orientation in composite laminates', *Materials Today: Proceedings*, Vol. 5, pp.5984–5992.

Mohammed, M.A., Abd Ghani, M.K., Hamed, R.I., Mostafa, S.A., Ahmad, M.S. and Ibrahim, D.A. (2017) 'Solving vehicle routing problem by using improved genetic algorithm for optimal solution', *Journal of Computational Science*, Vol. 21, pp.255–262.

Nikbakt, S., Kamarian, S. and Shakeri, M. (2018) 'A review on optimization of composite structures part I: laminated composites', *Composite Structures*, Vol. 195, pp.158–185.

Peikun, S. and Zhenpo, W. (2016) 'Research of the relationship between li-ion battery charge performance and SOH based on MIGA-gpr method', *Energy Procedia*, Vol. 88, pp.608–613.

Qian, L., Paredes, M., Wierzbicki, T., Sparrer, Y. and Feuerstein, M. (2016) 'Experimental and numerical study on shear-punch test of 6060 T6 extruded aluminum profile', *International Journal of Mechanical Sciences*, Vol. 118, pp.205–218.

Seo, J., Ooka, R., Kim, J.T. and Nam, Y. (2014) 'Optimization of the HVAC system design to minimize primary energy demand', *Energy and Buildings*, Vol. 76, pp.102–108.

Solis, A., Sánchez-Sáez, S. and Barbero, E. (2018) 'Influence of ply orientation on free-edge effects in laminates subjected to in-plane loads', *Composites Part B: Engineering*, Vol. 153, pp.149–158.

Soni, S. and Pradhan, S.K. (2019) 'Improving crash worthiness and dynamic performance of frontal plastic automotive body components', *Materials Today: Proceedings*, https://doi.org/10.1016/j.matpr.2019.09.118

Sun, G., Pang, T., Fang, J., Li, G. and Li, Q. (2017) 'Parameterization of criss-cross configurations for multiobjective crashworthiness optimization', *International Journal of Mechanical Sciences*, Vols. 124–125, pp.145–157.

Tanlak, N., Sonmez, F.O. and Senaltun, M. (2015) 'Shape optimization of bumper beams under high-velocity impact loads', *Engineering Structures*, Vol. 95, pp.49–60.

Tian, D. and Shi, Z. (2018) 'MPSO: modified particle swarm optimization and its applications', *Swarm and Evolutionary Computation*, Vol. 41, pp.49–68.

Viana, F.A.C., Haftka, R.T. and Watson, L.T. (2013) 'Efficient global optimization algorithm assisted by multiple surrogate techniques', *Journal of Global Optimization*, Vol. 56, pp.669–689.

Weimin, S., Weizhong, C. and Yeqing, G. (2019) 'Research on antenna cabin structure optimization based on response surface and multi-island genetic algorithm', *IOP Conference Series: Materials Science and Engineering*, Vol. 575, p.012018.

Xiong, F., Wang, D., Ma, Z., Chen, S., Lv, T. and Lu, F. (2018) 'Structure–material integrated multi-objective lightweight design of the front end structure of automobile body', *Structural and Multidisciplinary Optimization*, Vol. 57, pp.829–847.

Zuo, W., Yu, J. and Saitou, K. (2016a) 'Stress sensitivity analysis and optimization of automobile body frame consisting of rectangular tubes', *International Journal of Automotive Technology*, Vol. 17, pp.843–851.

Zuo, W., Liu, J.E.X., Peng, Q., Deng, Y. and Zhu, H. (2016b) 'Orthogonal experimental design and fuzzy grey relational analysis for emitter efficiency of the microcylindrical combustor with a step', *Applied Thermal Engineering*, Vol. 103, pp.945–951.